Supporting Information for:

Light-induced Li extraction from LiMn$_2$O$_4$/TiO$_2$ in a water-in-salt electrolyte for photo-rechargeable batteries

Kohei Shimokawa,[*ab] Shogo Matsubara,[c] Akihiro Okamoto[de] and Tetsu Ichitsubo[*bf]

[a] *Frontier Research Institute for Interdisciplinary Sciences, Tohoku University, 6-3 Aramaki Aza Aoba, Aoba-ku, Sendai 980-8578, Japan*

[b] *Institute for Materials Research, Tohoku University, 2-1-1 Katahira, Aoba-ku, Sendai 980-8577, Japan*

[c] *Department of Life Science and Applied Chemistry, Graduate School of Engineering, Nagoya Institute of Technology, Gokiso-cho, Show-ku, Nagoya 466-8555, Japan*

[d] *International Center for Materials Nanoarchitectonics (WPI-MANA), National Institute for Materials Science, 1-1 Namiki, Tsukuba, Ibaraki 305-0044, Japan*

[e] *Graduate School of Chemical Sciences and Engineering, Hokkaido University, North 13 West 8, Kita-ku, Sapporo, Hokkaido 060-8628, Japan*

[f] *Advanced Science Research Center, Japan Atomic Energy Agency, 2-4 Shirakata, Tokai-mura, Naka-gun, Ibaraki 319-1195, Japan*

* *E-mail: kohei.shimokawa.b7@tohoku.ac.jp; tichi@imr.tohoku.ac.jp*

Methods

Materials synthesis

Nanocrystalline $LiMn_2O_4$ was synthesized by the solution combustion method.[S1] $LiNO_3$, $Mn(NO_3)_2 \cdot 6H_2O$, and citric acid, purchased from Wako Chemicals, were dissolved in deionized water, and heated with a hotplate. After completing the evaporation of water, the temperature of the hotplate was suddenly increased to ignite the gel. The obtained material was heat treated with an electric muffle furnace in an air atmosphere for 4 hours at each temperature. The powder after calcination was hand-milled and filtered before making composite electrodes.

Materials characterizations

Crystal structures of the synthesized material were characterized by XRD and Rietveld analysis. An X-ray diffractometer (Rigaku, SmartLab) with Cu-$K\alpha$ radiation at the NIMS Battery Research Platform was used to obtain XRD profiles. VESTA[S2] was used for visualization of the crystal structure of spinel $LiMn_2O_4$ shown in Fig. 1b in the manuscript. Rietveld analysis was carried out with the program RIETAN-FP.[S3] The distribution of particle size for the synthesized $LiMn_2O_4$ particles dispersed in water was analyzed by using a nanoparticle tracking analyzer (Particle Metrix, ZetaView). The morphology of the $LiMn_2O_4$ was investigated with a scanning electron microscope (JEOL, JSM-7800F) at the NIMS Battery Research Platform. The composition of materials before/after the photocharging process was determined by ICP analysis at Analytical Research Core for Advanced Materials, Institute for Materials Research, Tohoku University. The XANES spectra were obtained at BL-12C, Photon Factory (PF), Japan. Boron nitride powder (Mitsuwa Chemicals, 99.5%) was used to dilute the materials for making pellets that are suitable for XANES experiments.

Multichannel screen-printed electrodes purchased from DropSens were employed to investigate the oxidative stability of $LiTFSA/H_2O$ electrolytes depending on the concentration. The working, counter, and reference electrodes are Au, Au, and Ag pastes, respectively. $LiTFSA/H_2O$ solutions with different concentrations were prepared by dissolving LiTFSA salt (Kishida Chemical, battery grade) into distilled water (Sigma-Aldrich). 150 μl of each electrolyte was used to obtain CV profiles shown in Fig. 2b in the manuscript. The CV profiles of $LiMn_2O_4$ on screen-printed electrodes (Fig. S4) were obtained by attaching the composite electrode consisting of $LiMn_2O_4$, carbon black, and PVdF to the Au working electrode with an Al conductive tape.

AgNO$_3$ (Sigma-Aldrich, >99%), $K_2Cr_2O_7$ (Sigma-Aldrich, >99%), and $K_2S_2O_8$ (Sigma-Aldrich, >99%) were used for electron acceptors. CV measurements were carried out to check their electrochemical activity in 21 M $LiTFSA/H_2O$ electrolyte by using a beaker-type cell connected with a galvanostat/potentiostat (Biologic, SP200). Pt foil, Pt mesh, and Ag/AgCl in saturated KCl aqueous solution were used for the working, counter, and reference electrodes, respectively. The CV profiles for showing the cyclability of $LiMn_2O_4$ in 21 M $LiTFSA/H_2O$ (Fig. 2c in the manuscript) were obtained with the same electrochemical setup, whereas the working electrode was the composite electrode of $LiMn_2O_4$, carbon black, and PVdF in a weight ratio of 8:1:1 with Al current corrector.

Photo-electrochemical experiments

A xenon light source (Asahi Spectra, MAX-350) was used for illuminating UV-visible light to the electrode in a beaker-type cell as illustrated in Fig. S7. The intensity of UV-visible light was ~0.36 W/cm^2, and the wavelength is 300–600 nm. Anatase TiO_2 (JRC-TIO-10; reference catalyst, The Catalysis Society of Japan) with a particle size of ~15 nm was used to make the composite electrode of $LiMn_2O_4$, TiO_2, carbon black, and PVdF in a weight ratio of 4:4:1:1 with Al current corrector. The area of the composites on Al current corrector was 1 cm^2. Pt mesh and Ag/AgCl electrode immersed in saturated KCl aqueous solution were employed for the counter and reference electrodes, respectively. The reference electrode was wrapped with Teflon tape to prevent degradation by illumination. A glass cup used for the beaker-type cell was placed on a Cu-metal block to alleviate the heating of the cell during photo-electrochemical measurements. All electrochemical experiments were conducted inside a blackout curtain to avoid any lights except the xenon lamp. The light was turned on typically 10 minutes after constructing the cell to wait for the impregnation of the composite electrode with the electrolyte. The potential change in the reference electrode was within 10 mV before/after each experiment.

Table S1. Comparison of the selection of materials in previous papers (Refs. 1–10 in the manuscript) and this work. Although TiO_2 is a famous photocatalyst, it also allows Li insertion; therefore, TiO_2 is used in Refs. 1 and 2 as the cathode material. $LiFePO_4$ used in Ref. 3 is one of the representative cathode materials in the field of Li-ion batteries. Its high stability is advantageous, but one drawback is the relatively low potential compared to $LiMn_2O_4$- and $LiCoO_2$-based 4 V class cathode materials. Redox reactions of iodine and sulfur are used as cathode and anode, respectively, in Ref. 6, which is like the concept of redox-flow batteries. Vanadium oxides are employed in Refs. 8–10. This is also a smart strategy because they are robust and have suitable bandgaps for photo-rechargeable batteries. As shown in this table, photocharging of 4 V class cathode material is still challenging. The water-in-salt electrolyte (*i.e.*, 21 M $LiTFSA/H_2O$) is a key to exploring high-potential cathode materials due to its excellent oxidative stability compared to dilute aqueous electrolyte. Although organic solvent-based electrolytes also have wide electrochemical windows, their flammability is a concern especially for photo-rechargeable batteries because they are exposed to light, unlike conventional Li-ion batteries.

	Cathode material	Potential of cathode material (vs. Li^+/Li)	Photoactive material	Electrolyte
Ref. 1	TiO_2	1.5–2.5 V	TiO_2	1 M $LiPF_6$ in EC/DMC
Ref. 2	TiO_2	1.5–2.5 V	TiO_2	EC/DMC- or EMI.TFSA-based electrolyte
Ref. 3	$LiFePO_4$	~3.4 V	Ru dye N719	1 M $LiPF_6$ in EC/DEC
Ref. 4	Cu_2S	1.6–2.6 V	dye-sensitized TiO_2	LiTFSA electrolyte
Ref. 5	Polyaniline[a]	_[a]	TiO_2	1 M $HClO_4$ in H_2O
Ref. 6	I^-/I_3^-	~3.6 V	SnS_2	Na_2S_4/NaI in H_2O
Ref. 7	2D perovskite	1–3 V	2D perovskite	1 M $LiPF_6$ electrolyte
Ref. 8	V_2O_5	3–3.5 V[b]	V_2O_5	3 M $Zn(CF_3SO_3)_2$ in H_2O
Ref. 9	V_2O_5	3–3.5 V	V_2O_5	1 M or 5 M LiTFSA electrolyte
Ref. 10	VO_2	2.5–3.5 V[b]	VO_2	3 M $Zn(CF_3SO_3)_2$ in H_2O
This work	$LiMn_2O_4$	~4 V	TiO_2	21 M LiTFSA in H_2O

[a]Ref. 5 demonstrates the dedoping of anion from polyaniline; thus, the potential is not shown in this table.
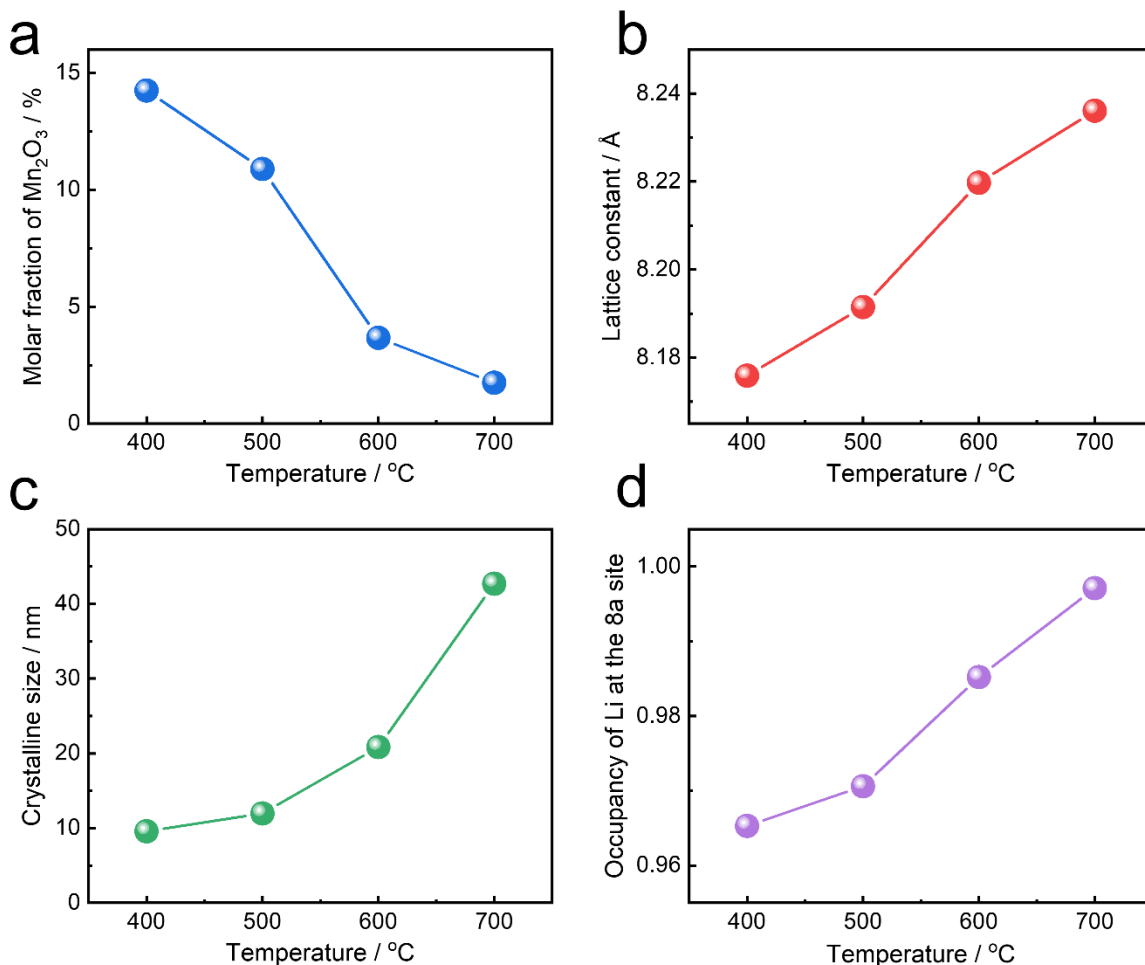[b]Although Refs. 8 and 10 are for Zn-ion batteries, the potentials are roughly converted to be based on Li.

Figure S1. Summary of the results of Rietveld analysis for the synthesized $LiMn_2O_4$ depending on the calcination temperature, for the following structure parameters: (a) Molar fraction of impurity Mn_2O_3, (b) lattice constant of $LiMn_2O_4$, (c) crystalline size of $LiMn_2O_4$, and (d) occupancy of Li at the 8a site. The analysis was carried out with the program RIETAN-FP.[S3] It was assumed in the analysis that (i) there are no vacancies at the 8a and 16d sites, (ii) the molar ratio of Li/Mn was fixed to 1/2 (based on the ICP analysis), and (iii) there are two phases of $LiMn_2O_4$ and Mn_2O_3. The molar ratio of impurity Mn_2O_3 decreased at high temperatures, while the lattice constant of $LiMn_2O_4$ increased to approximately 8.24 Å at 700 °C. Because the lattice constant of stoichiometric $LiMn_2O_4$ is reported to be ~8.24 Å,[S4,S5] higher temperature would be better to synthesize $LiMn_2O_4$ with lower defects. In addition, the crystalline size increases with increasing the temperature. The particle size also increases especially at 700 °C as shown in Fig. S2 and S3, which is disadvantageous to achieving fast charge/discharge. The $LiMn_2O_4$ calcined at 600 °C was therefore used for electrochemical measurements shown in the manuscript. The ordering of Li and Mn between the 8a and 16d sites (*i.e.*, normal or inverse spinel) is also an important parameter since it largely affects diffusion pathways and activation energies.[S6] The synthesized $LiMn_2O_4$ was almost normal spinel, which allows the Li extraction/insertion via the 8a−16c−8a three-dimensional diffusion pathways.
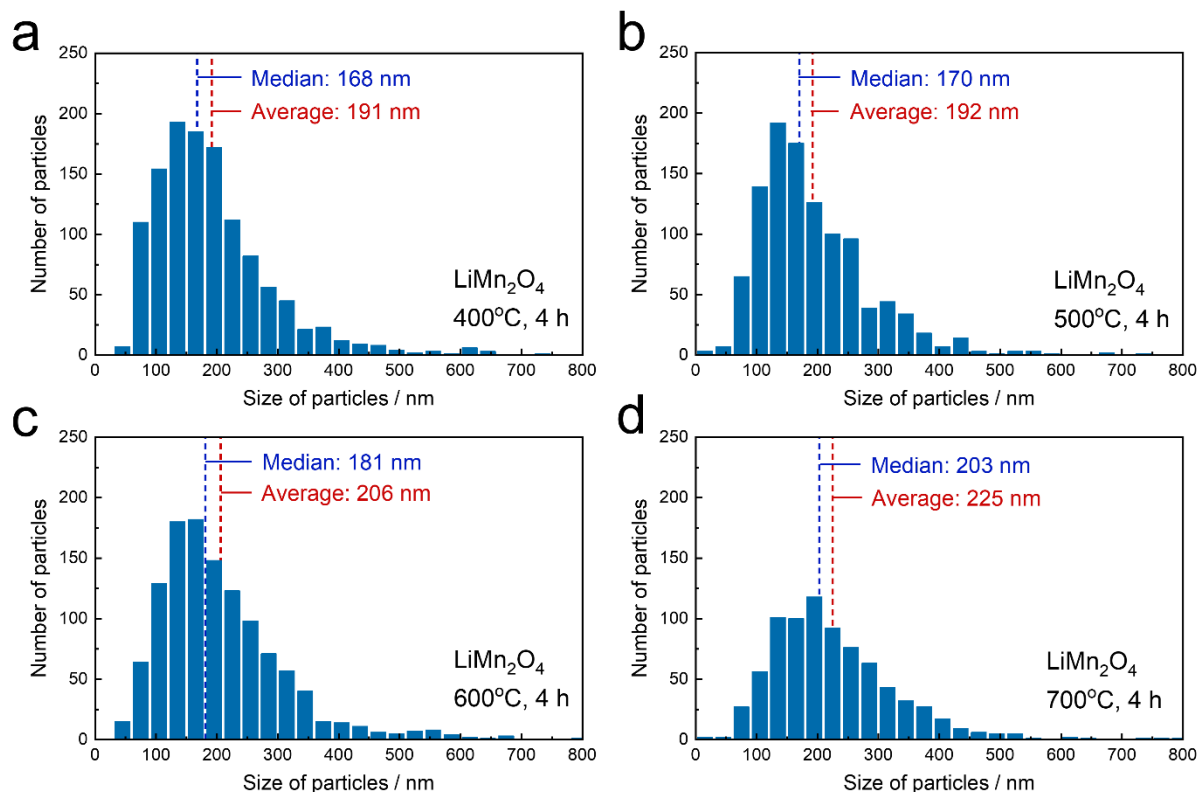
Figure S2. Distribution of particle size measured with a nanoparticle tracking analyzer (NTA) for the synthesized $LiMn_2O_4$ calcined at the temperatures of (a) 400 °C, (b) 500 °C, (c) 600 °C, and (d) 700 °C. The particles were dispersed in water to dilute 250,000 times, and the measurements were carried out just after ultrasonication. The values of median and average are also shown in each figure. There is no large difference in particle size between 400 °C and 500 °C. Although the median of the particle size increased to 181 nm for the material calcined at 600 °C, no large change in the distribution of particles was observed compared to those calcined at lower temperatures. In contrast, the numbers of small particles around 100 nm were significantly decreased when calcined at 700 °C, resulting in the median value of above 200 nm. Such an increase in particle size was also indicated by SEM observation, as shown in Fig. S3.
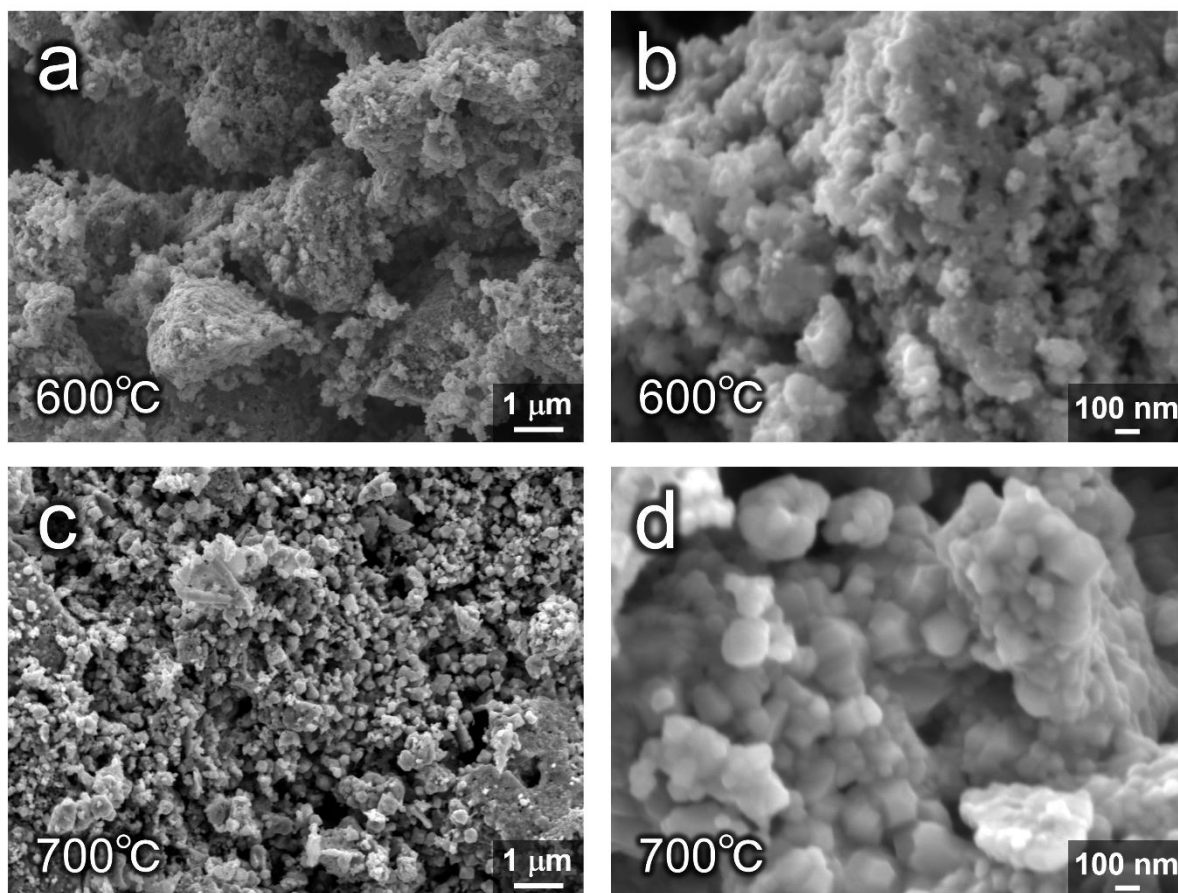
Figure S3. SEM images for the synthesized LiMn$_2$O$_4$ calcined at (a,b) 600 °C and (c,d) 700 °C. The particle size of the material calcined at 600 °C is typically 100−200 nm, while they are aggregated. The particle size clearly increased by the calcination at 700 °C. Although the primary particles would be around 100 nm, the secondary particles are much larger than them. The above results are consistent with the result obtained with NTA shown in Fig. S2.
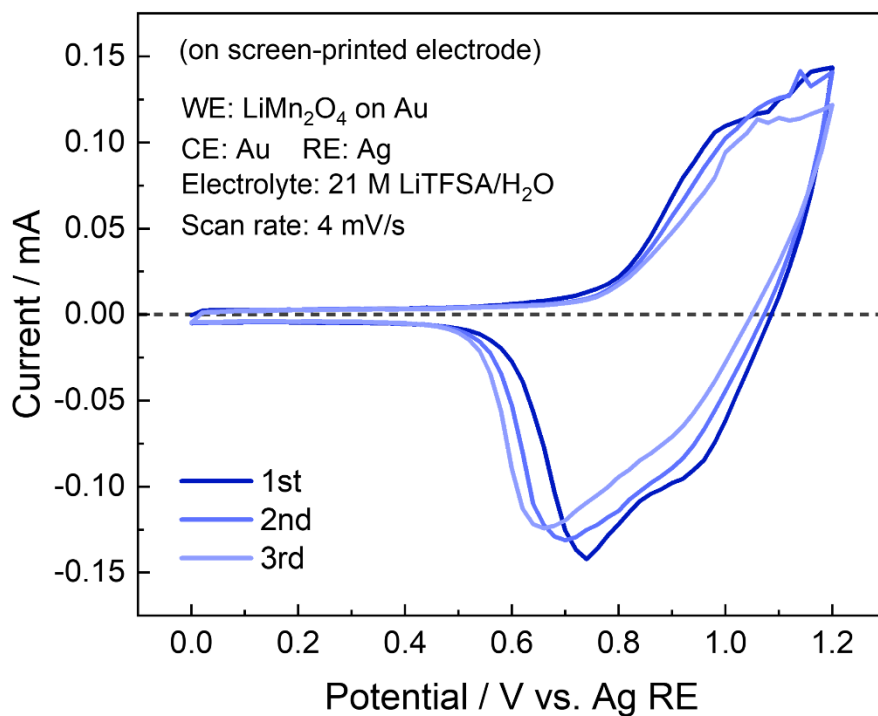
Figure S4. CV profiles for the composite electrode of LiMn₂O₄ obtained by using screen-printed electrodes. The charge/discharge behavior is basically consistent with that in a beaker-type cell (Fig. 2c in the manuscript). Because the reference electrode is Ag paste, not Ag/AgCl in saturated KCl used in our beaker-type cells, the charge/discharge potential is slightly different between them, whereas the difference is within approximately 0.1 V. The oxidation limit of 21 M LiTFSA/H₂O is higher than 1.2 V vs. Ag RE (Fig. 2b, inset), enabling the reversible charge/discharge of LiMn₂O₄.
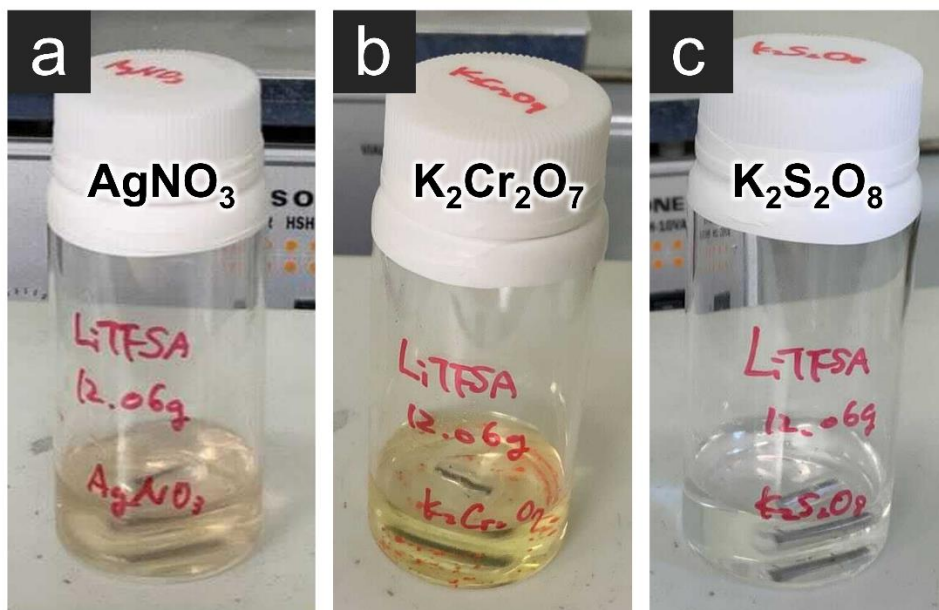
Figure S5. Digital photographs for the 21 M LiTFSA/H$_2$O electrolytes with the following electron acceptors: (a) AgNO$_3$, (b) K$_2$Cr$_2$O$_7$, and (c) K$_2$S$_2$O$_8$. 50 mM of each electron acceptor was put into the solution of 21 M LiTFSA/H$_2$O and stirred overnight at room temperature. Note that the concentration of 50 mM is only based on the amount of water used for making 21 M LiTFSA/H$_2$O, whereas the volume of the electrolyte is much higher than it. AgNO$_3$ and K$_2$S$_2$O$_8$ were completely dissolved at room temperature, while the orange-colored solid K$_2$Cr$_2$O$_7$ remained on the bottom. Although we kept stirring for several days at elevated temperatures, it was difficult to completely dissolve it. Because K$_2$Cr$_2$O$_7$ can dissolve into water, such a low dissolubility is probably due to the high concentration of the 21 M LiTFSA/H$_2$O solution, where free water molecules are limited.
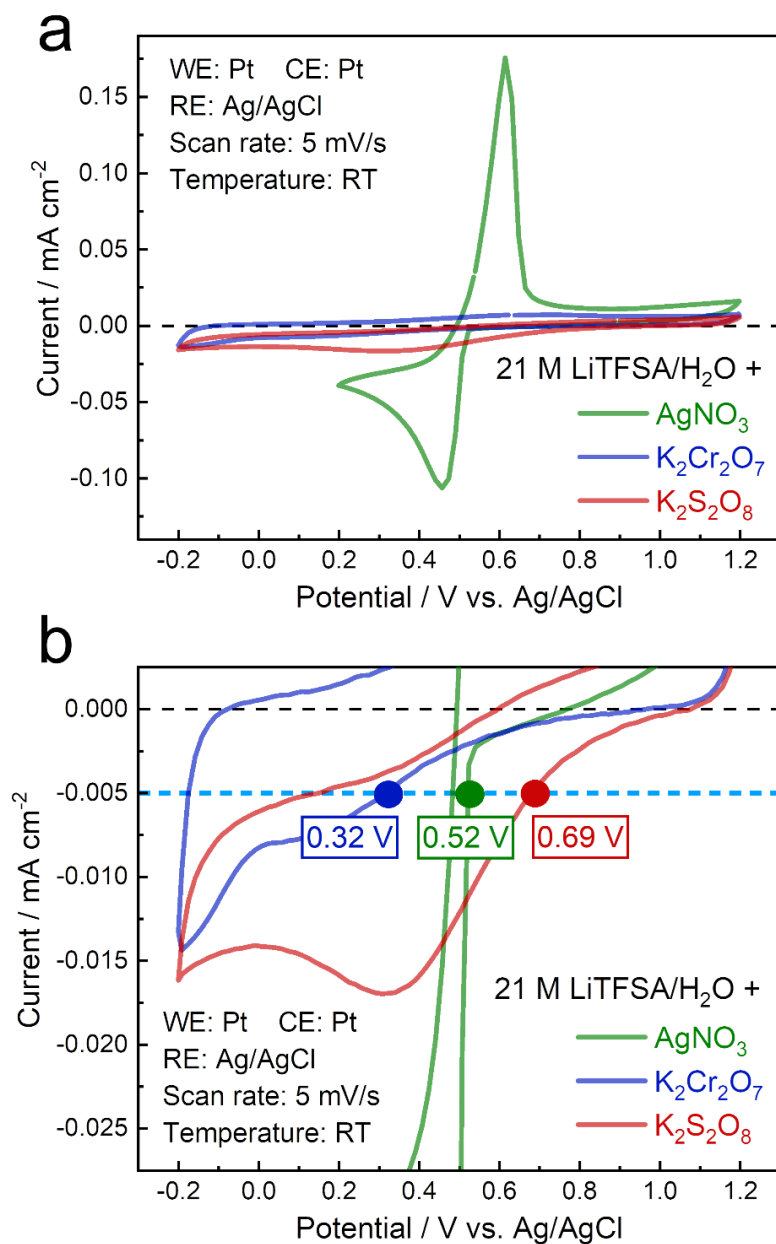
Figure S6. (a) CV profiles for the 21 M LiTFSA/H_2O electrolytes with the electron acceptors of $AgNO_3$, $K_2Cr_2O_7$, and $K_2S_2O_8$, and (b) their enlarged view. Pt foil, Pt mesh, and Ag/AgCl electrode in saturated KCl were employed for the working, counter, and reference electrodes, respectively. The reductive current for $AgNO_3$ was much higher than those for the other electron acceptors because it is a simple deposition reaction of Ag metal. A low reductive current was observed for $K_2Cr_2O_7$ probably due to its low solubility as shown in Fig. S5. Although the maximum reductive current from $K_2S_2O_8$ was lower than that of Ag deposition, the potential to achieve 5 μA/cm^2 was as high as 0.69 V vs. Ag/AgCl.
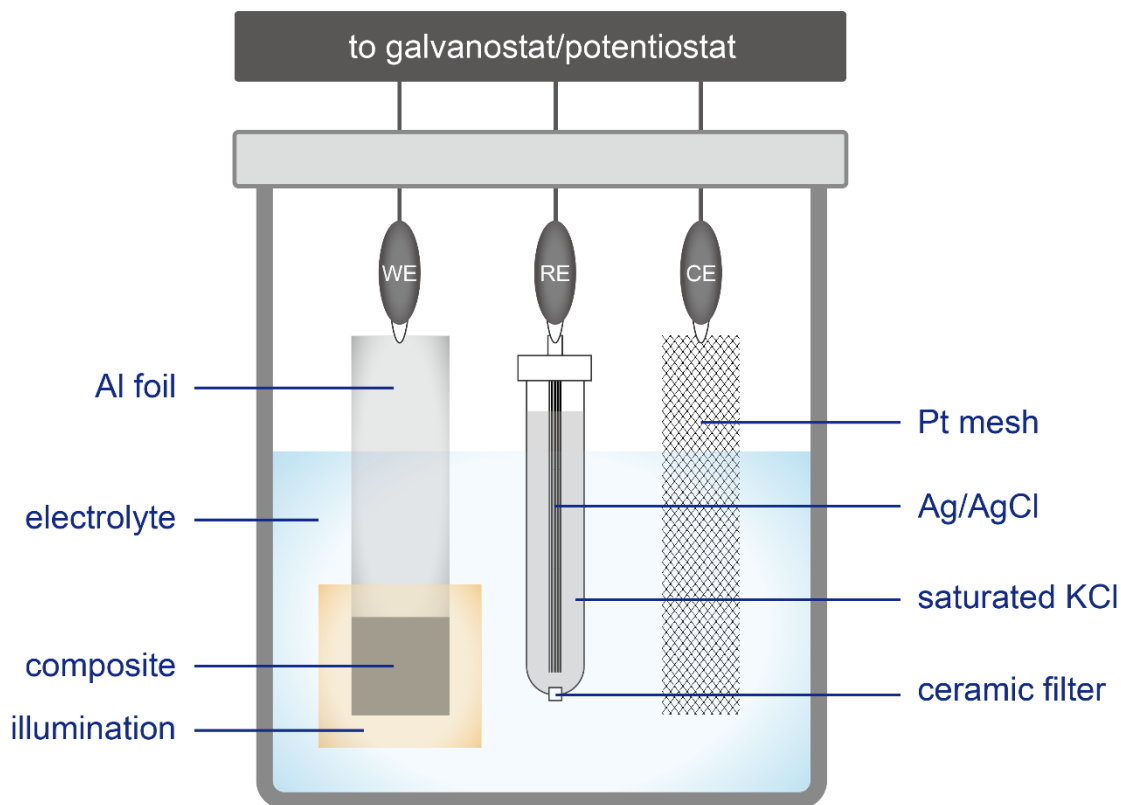
Figure S7. Schematic illustration showing the three-electrode beaker-type cell employed for photo-electrochemical experiments. Composite electrode consisting of $LiMn_2O_4$, TiO_2, carbon black, and PVdF pasted on Al current corrector was used for the working electrode. The area of the composite is 1 cm^2. UV-visible light from a xenon lamp was illuminated to the composite. Ag/AgCl reference electrode soaked in saturated KCl aqueous solution was separated from the electrolyte with a ceramic filter. The reference electrode was wrapped with Teflon tape for preventing degradation by illumination. Pt mesh was used as the counter electrode. The cell was placed in a blackout curtain to avoid any lights except the xenon lamp.
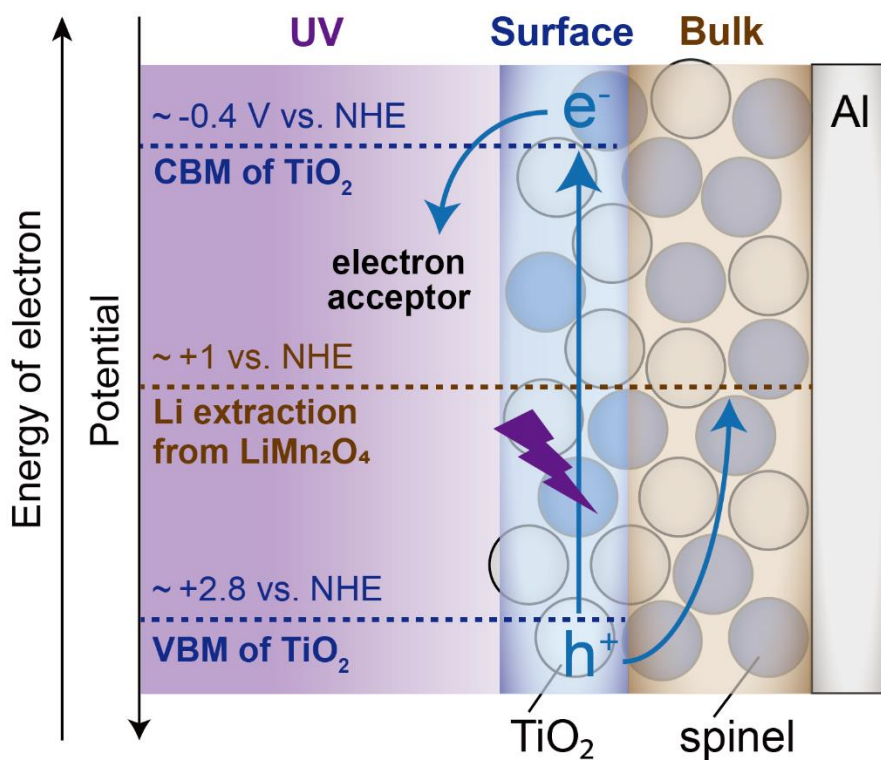
Figure S8. Schematic illustration showing the photocharging mechanism utilizing TiO_2 and electron acceptor. The valence band maximum (VBM) and conduction band minimum (CBM) of anatase TiO_2 are approximately +2.8 V and -0.4 V vs. NHE, respectively, according to previous reports. On the other hand, the potential for Li extraction from $LiMn_2O_4$ is approximately +1 V vs. NHE. It is, therefore, energetically possible to drive Li extraction from $LiMn_2O_4$ by the excitation of the electrons in TiO_2 under illumination in using electron acceptors.
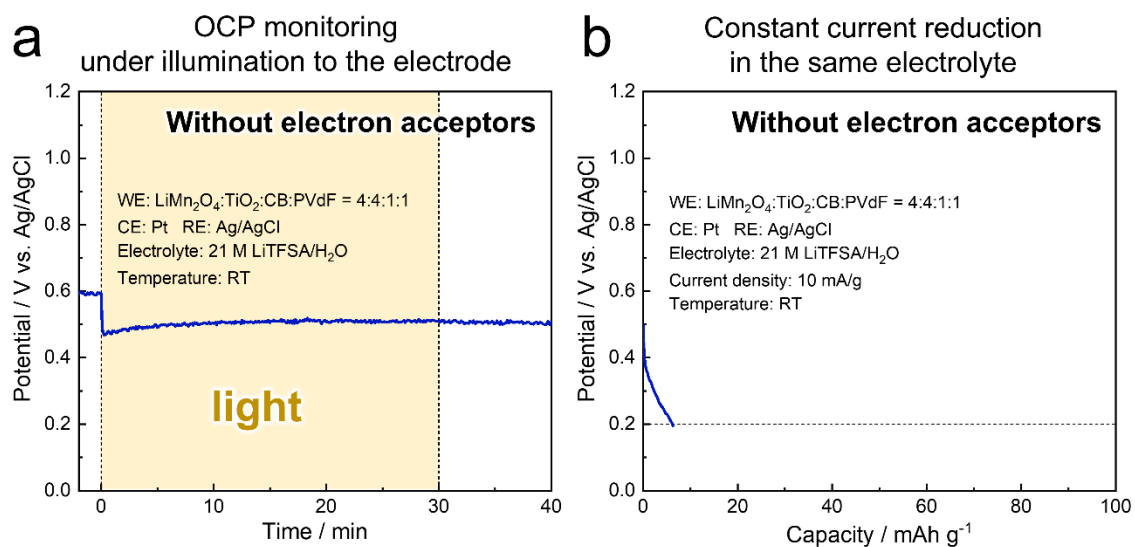
a OCP monitoring under illumination to the electrode

Without electron acceptors

WE: LiMn$_2$O$_4$:TiO$_2$:CB:PVdF = 4:4:1:1
CE: Pt   RE: Ag/AgCl
Electrolyte: 21 M LiTFSA/H$_2$O
Temperature: RT

light

Potential / V vs. Ag/AgCl
Time / min

b Constant current reduction in the same electrolyte

Without electron acceptors

WE: LiMn$_2$O$_4$:TiO$_2$:CB:PVdF = 4:4:1:1
CE: Pt   RE: Ag/AgCl
Electrolyte: 21 M LiTFSA/H$_2$O
Current density: 10 mA/g
Temperature: RT

Potential / V vs. Ag/AgCl
Capacity / mAh g^{-1}

Figure S9. (a) OCP profile under illumination to the composite electrode of LiMn$_2$O$_4$/TiO$_2$ in 21 M LiTFSA/H$_2$O without electron acceptors and (b) potential change during constant current reduction (corresponding to discharge for cathode) in the same electrolyte. The OCP suddenly decreased just after illumination, whereas the potential kept almost constant after that. The obtained discharging capacity in the subsequent constant current measurement was less than 10 mAh/g.
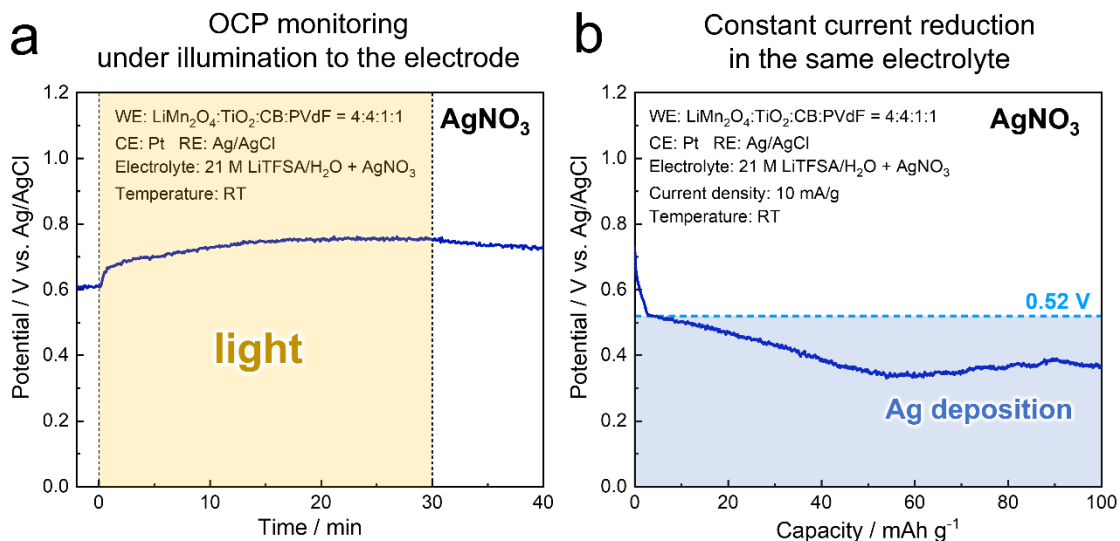
a

OCP monitoring under illumination to the electrode

WE: LiMn$_2$O$_4$:TiO$_2$:CB:PVdF = 4:4:1:1
CE: Pt   RE: Ag/AgCl
Electrolyte: 21 M LiTFSA/H$_2$O + AgNO$_3$
Temperature: RT

AgNO$_3$

light

Potential / V vs. Ag/AgCl
Time / min

b

Constant current reduction in the same electrolyte

WE: LiMn$_2$O$_4$:TiO$_2$:CB:PVdF = 4:4:1:1
CE: Pt   RE: Ag/AgCl
Electrolyte: 21 M LiTFSA/H$_2$O + AgNO$_3$
Current density: 10 mA/g
Temperature: RT

AgNO$_3$

0.52 V

Ag deposition

Potential / V vs. Ag/AgCl
Capacity / mAh g^{-1}

Figure S10. (a) OCP profile under illumination to the composite electrode of LiMn$_2$O$_4$/TiO$_2$ in 21 M LiTFSA/H$_2$O with AgNO$_3$ and (b) potential change during constant current reduction (corresponding to discharge for cathode) in the same electrolyte. The potential was increased to around 0.75 V vs. Ag/AgCl in contrast to Fig. S9. This result indicates that both the Ag deposition[S7,S8] due to the excited electrons in TiO$_2$ and the oxidation of LiMn$_2$O$_4$ by holes proceed simultaneously, because the potential, 0.75 V vs. Ag/AgCl, is almost the average of the potentials of deposited Ag metal (~0.5 V vs. Ag/AgCl; Fig. S6) and Li$_{1-x}$Mn$_2$O$_4$ (~1.0 V vs. Ag/AgCl; Fig. 2c in the manuscript) in the electrolyte; in other words, we probably observed a mixed potential of them. In the following constant current experiment, electrochemical Ag deposition from the electrolyte was observed at the potentials below 0.52 V vs. Ag/AgCl, which is consistent with the CV profile for this electrolyte (Fig. S6b).
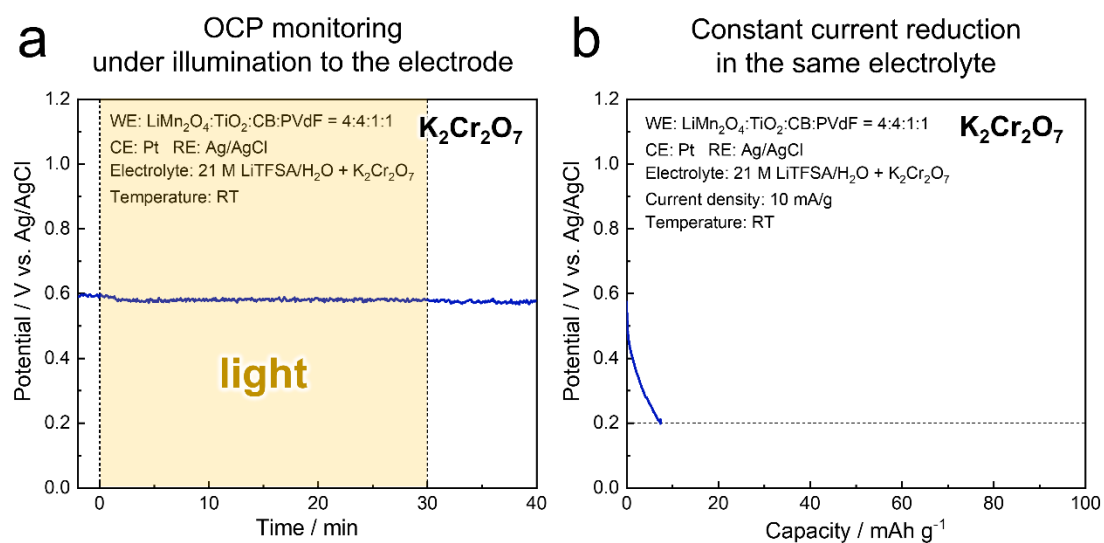
a OCP monitoring under illumination to the electrode

WE: LiMn$_2$O$_4$:TiO$_2$:CB:PVdF = 4:4:1:1
CE: Pt RE: Ag/AgCl
Electrolyte: 21 M LiTFSA/H$_2$O + K$_2$Cr$_2$O$_7$
Temperature: RT

K$_2$Cr$_2$O$_7$

light

b Constant current reduction in the same electrolyte

WE: LiMn$_2$O$_4$:TiO$_2$:CB:PVdF = 4:4:1:1
CE: Pt RE: Ag/AgCl
Electrolyte: 21 M LiTFSA/H$_2$O + K$_2$Cr$_2$O$_7$
Current density: 10 mA/g
Temperature: RT

K$_2$Cr$_2$O$_7$

Figure S11. (a) OCP profile under illumination to the composite electrode of LiMn$_2$O$_4$/TiO$_2$ in 21 M LiTFSA/H$_2$O with K$_2$Cr$_2$O$_7$ and (b) potential change during constant current reduction (corresponding to discharge for cathode) in the same electrolyte. The OCP was almost constant even after illumination, as predicted by low electrochemical activity in CV measurement (Fig. S6) probably due to its low solubility in the highly concentrated electrolyte. The discharge capacity obtained in the subsequent constant current test was less than 10 mAh/g, which is like the case without electron acceptors (Fig. S9).
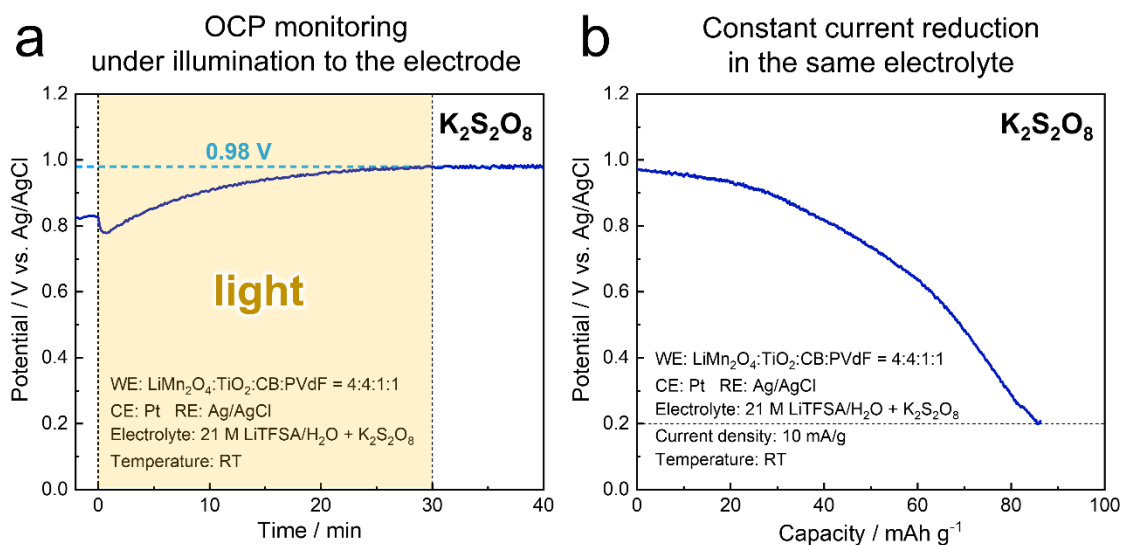
Figure S12. (a) OCP profile under illumination to the composite electrode of $LiMn_2O_4/TiO_2$ in 21 M $LiTFSA/H_2O$ with $K_2S_2O_8$ and (b) potential change during constant current reduction (corresponding to discharge for cathode) in the same electrolyte. The OCP was significantly increased under illumination and reached approximately 1 V vs. Ag/AgCl, which is the potential for Li extraction from $LiMn_2O_4$; see Fig. 2c in the manuscript. The potential became constant after turning the light off, also indicating that the charging of $LiMn_2O_4$ was driven by illumination. In the subsequent discharging process, the capacity of over 80 mAh/g was obtained; however, it involves electrochemical reduction of $K_2S_2O_8$ because the discharging test was conducted in the electrolyte containing $K_2S_2O_8$ used for the photocharging process. Nevertheless, the plateau around 1 V vs. Ag/AgCl suggests the Li intercalation reaction into $Li_{1-x}Mn_2O_4$. To measure the capacity only from $Li_{1-x}Mn_2O_4$, we have changed the electrolyte to pure 21 M $LiTFSA/H_2O$ without $K_2S_2O_8$ after the photocharging process, and the results are shown in Fig. 3b in the manuscript. The discharging capacity from $Li_{1-x}Mn_2O_4$ after the 30 min photocharging was 25 mAh/g, which is roughly consistent with the electric charging capacity to reach the same potential; see Fig. S13b.
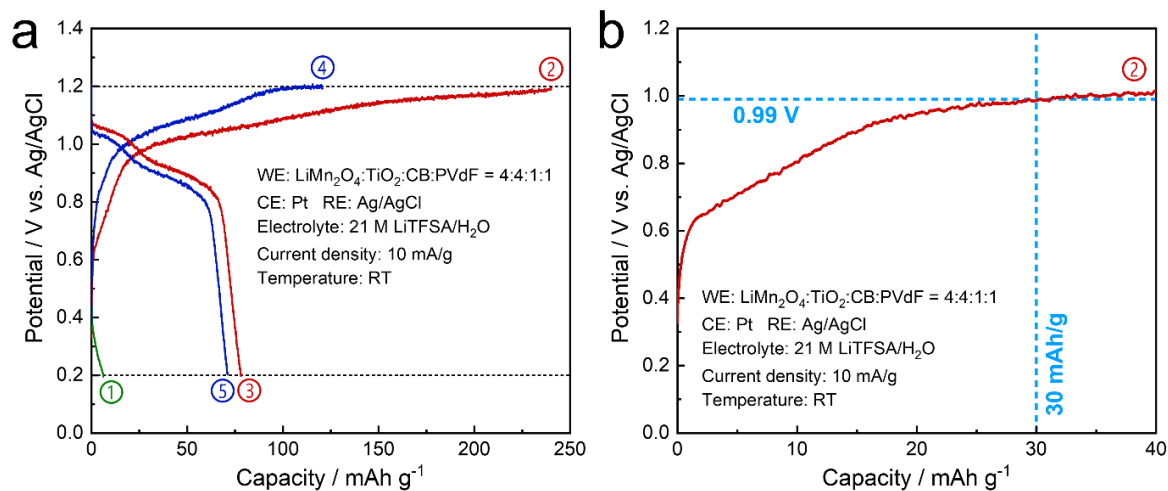
Figure S13. (a) Electric discharge/charge profiles for the composite electrode of $LiMn_2O_4/TiO_2$ in the electrolyte of 21 M $LiTFSA/H_2O$, and (b) an enlarged view for the first charging process. The charge and discharge proceed at around 1 V vs. Ag/AgCl, indicating the topotactic reaction of spinel $LiMn_2O_4$. The charging capacity is much higher than the discharge capacities, suggesting that electrolyte decomposition was involved in the charging process. As shown in the right figure, the charging capacity until 0.99 V vs. Ag/AgCl is ~30 mAh/g. Considering the electrolyte decomposition involved in the charging capacity, this value is roughly consistent with the result of the photocharge/discharge experiment (Fig. 3 in the manuscript), where the discharging capacity of 25 mAh/g was obtained from the OCP of 0.99 V vs. Ag/AgCl after 30 min photocharging.
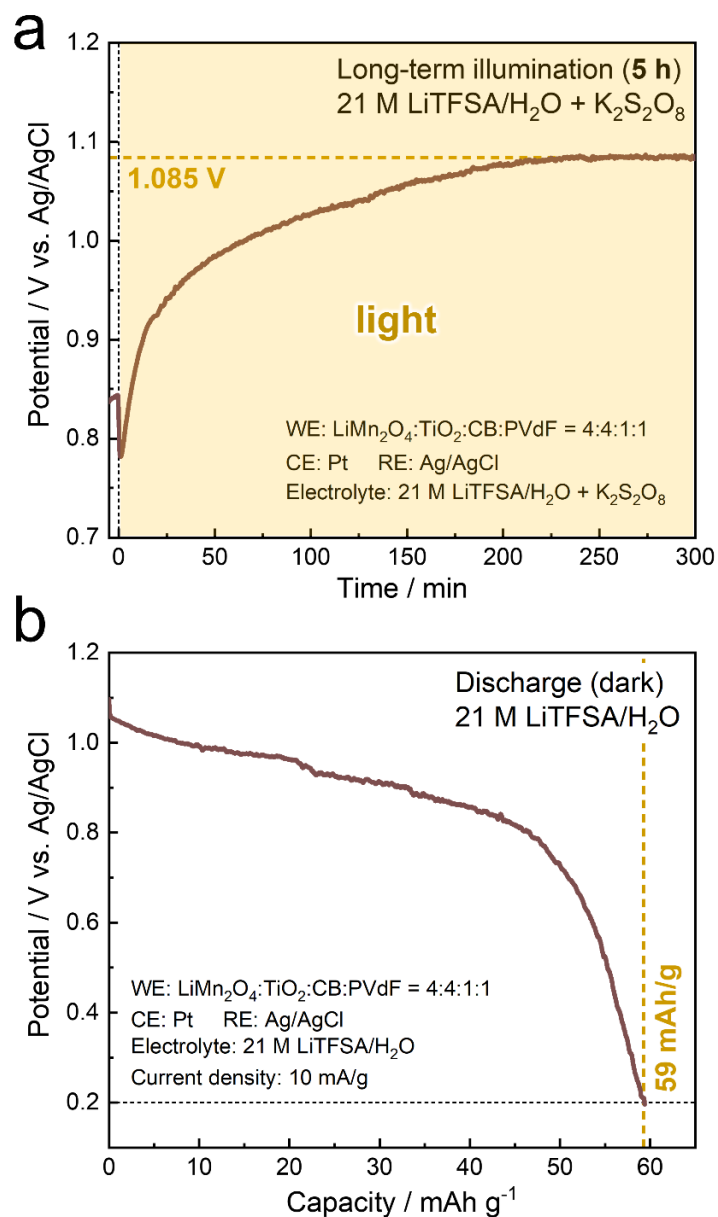
Figure S14. (a) OCP profile for the composite electrode of $LiMn_2O_4/TiO_2$ under 5-h-long illumination in the electrolyte of 21 M $LiTFSA/H_2O$ with $K_2S_2O_8$, and (b) the potential change during the subsequent discharging process at 10 mA/g after replacing the electrolyte with 21 M $LiTFSA/H_2O$ lacking electron acceptors. The potential profile under illumination exhibited a plateau at ~1.085 V vs. Ag/AgCl, which might be the maximum potential that $LiMn_2O_4/TiO_2$ electrode can reach in this system. In the following discharge process, a large capacity was observed at around 1 V vs, Ag/AgCl, indicating the Li intercalation into $Li_{1-x}Mn_2O_4$. The total discharging capacity was as high as 59 mAh/g, which is approximately 40% of the theoretical capacity of $LiMn_2O_4$ (*i.e.*, 148 mAh/g).
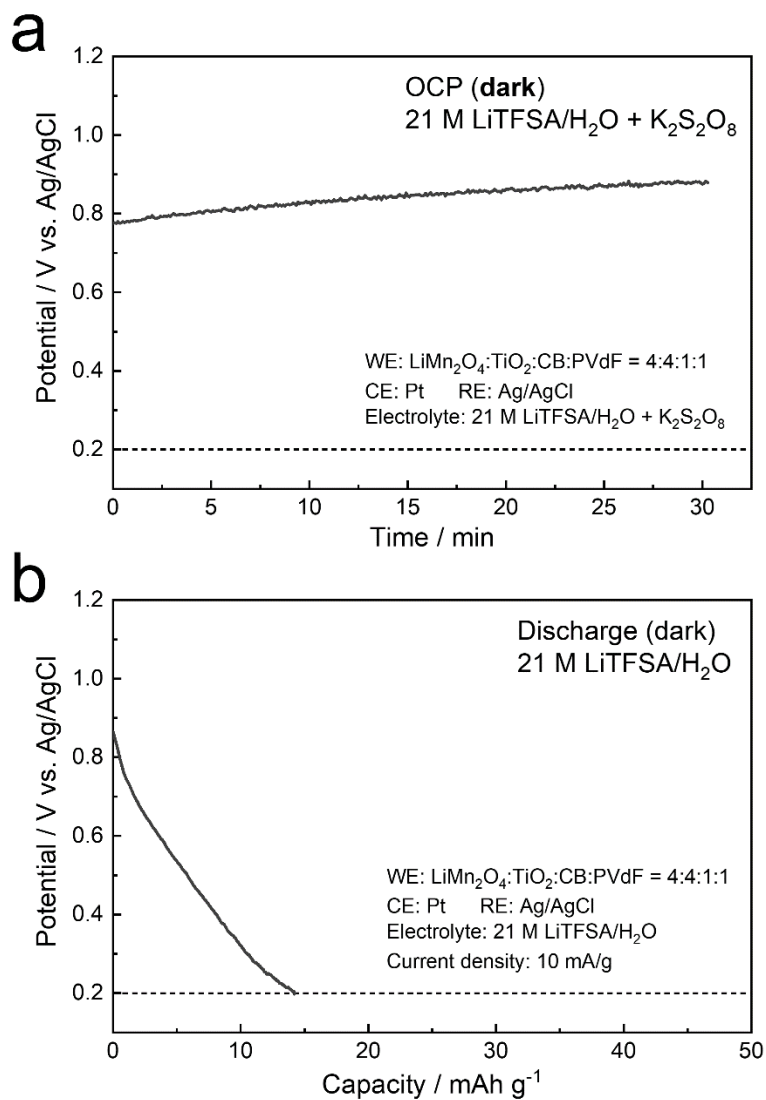
Figure S15. (a) OCP profile for the composite electrode of $LiMn_2O_4/TiO_2$ without illumination in the electrolyte of 21 M $LiTFSA/H_2O$ with $K_2S_2O_8$, and (b) the potential change during the subsequent discharging process at 10 mA/g after replacing the electrolyte with 21 M $LiTFSA/H_2O$ lacking electron acceptors. The OCP did not reach around 1 V vs. Ag/AgCl even after 30 min soaking without illumination, resulting in no discharge capacity at around 1 V vs. Ag/AgCl, unlike Fig. 3 in the manuscript. The above results indicate that the substantial Li extraction from bulk $LiMn_2O_4$ is difficult without illumination at least in this time scale.
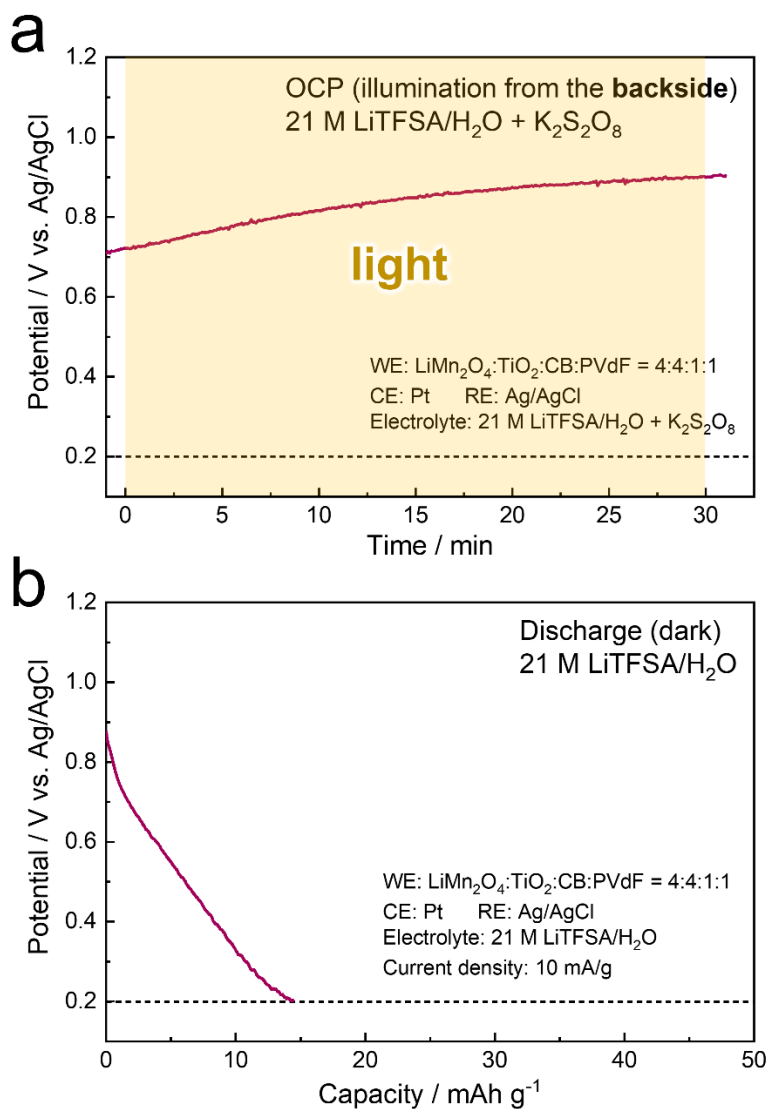
Figure S16. (a) OCP profile for the composite electrode of $LiMn_2O_4/TiO_2$ under illumination from the backside of the electrode, namely, illumination to the Al current corrector, in the electrolyte of 21 M $LiTFSA/H_2O$ with $K_2S_2O_8$, and (b) the potential change during the subsequent discharging process at 10 mA/g after replacing the electrolyte with 21 M $LiTFSA/H_2O$ lacking electron acceptors. The OCP did not reach around 1 V vs. Ag/AgCl like in the case without illumination (Fig. S15a), indicating that the thermal and optical effects on the electrolyte and/or the electron acceptor by illumination are not critical in our experiments. The capacity obtained in the subsequent discharging process was about 14 mAh/g, which is consistent with that in the experiment without illumination (Fig. S15b).
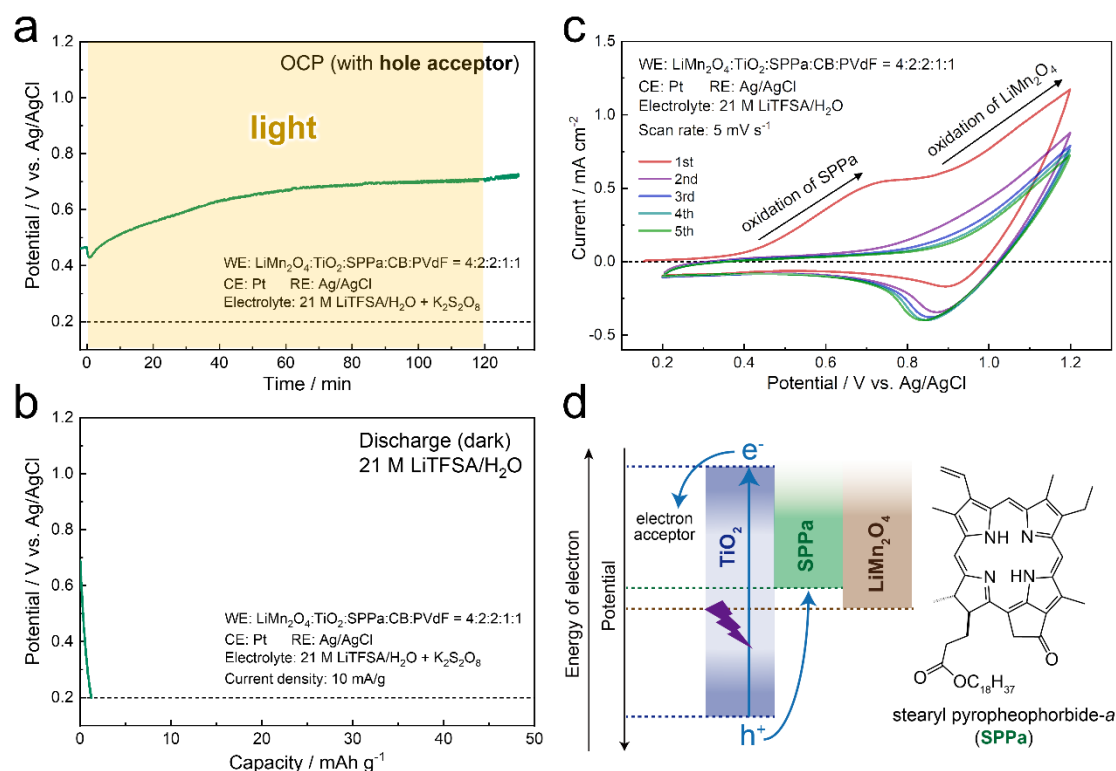
Figure S17. (a) OCP profile for the composite electrode of $LiMn_2O_4$/TiO_2/stearyl pyropheophorbide-*a* (SPPa) under illumination in the electrolyte of 21 M $LiTFSA/H_2O$ with $K_2S_2O_8$. (b) Discharging profile during the subsequent constant current reduction at 10 mA/g after replacing the electrolyte with 21 M $LiTFSA/H_2O$ lacking electron acceptors. (c) CV profiles at 5 mV/s for the composite electrode of $LiMn_2O_4$/TiO_2/SPPa in 21 M $LiTFSA/H_2O$ electrolyte. (d) Schematic illustration for explaining the photo-electrochemical reaction under illumination in the composite electrode involving SPPa as a hole acceptor (left) and the molecular structure of SPPa (right). In the CV measurement, an oxidation reaction appeared from ~0.5 V vs. Ag/AgCl before the oxidation of $LiMn_2O_4$ only in the first cycle, indicating that SPPa decomposed by electrochemical oxidation. This suggests that the HOMO level of SPPa is around ~0.5 V vs. Ag/AgCl. Because this potential is lower than that for Li extraction from $LiMn_2O_4$, SPPa plays a role in hole acceptor as illustrated in (d; left). Indeed, the increase in OCP was limited to below approximately 0.7 V vs. Ag/AgCl under illumination, and the capacity in the following discharge process was negligible.
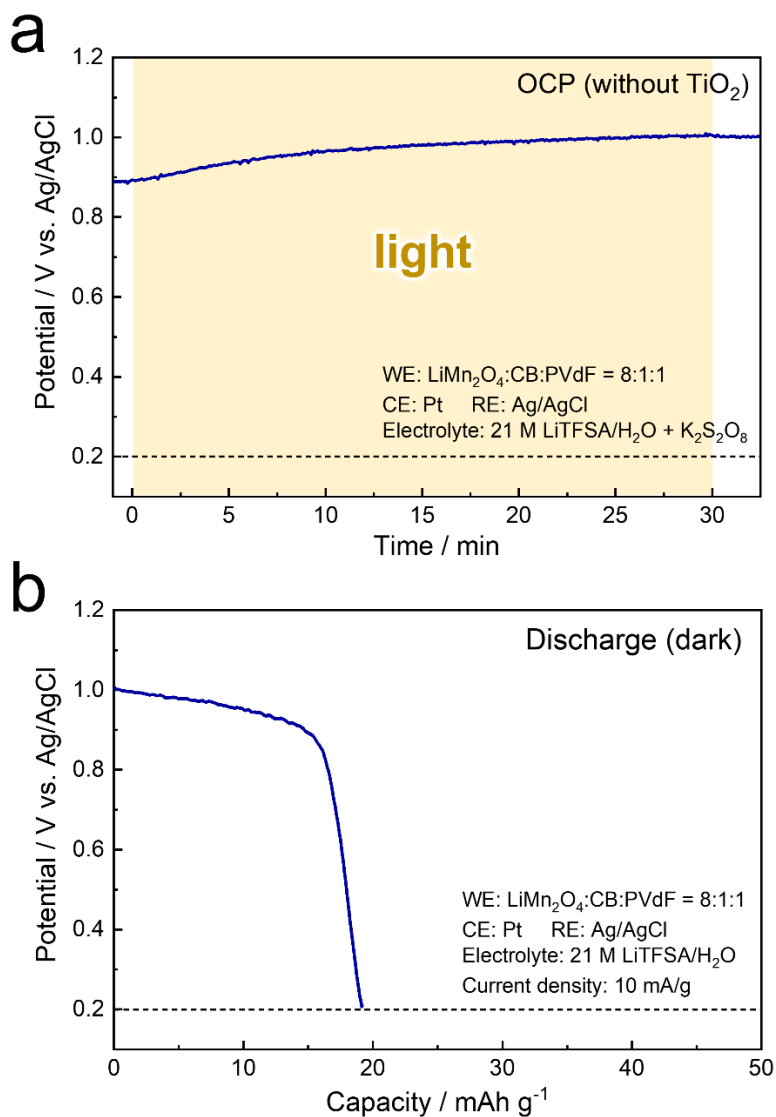
Figure S18. (a). OCP profile under illumination for the composite electrode of $LiMn_2O_4$ without TiO_2 in the electrolyte of 21 M $LiTFSA/H_2O$ with $K_2S_2O_8$, and (b) the potential change during the subsequent discharging process at 10 mA/g after replacing the electrolyte with 21 M $LiTFSA/H_2O$ lacking electron acceptors. Photocharging was indicated even without TiO_2 because $K_2S_2O_8$ can also accept the electrons excited in $LiMn_2O_4$; however, the obtained capacity was only 19 mAh/g, which is lower than that for the composite electrode consisting of $LiMn_2O_4/TiO_2$ (*i.e.*, 25 mAh/g). This suggests that using TiO_2 is effective for increasing the efficiency of photocharging.

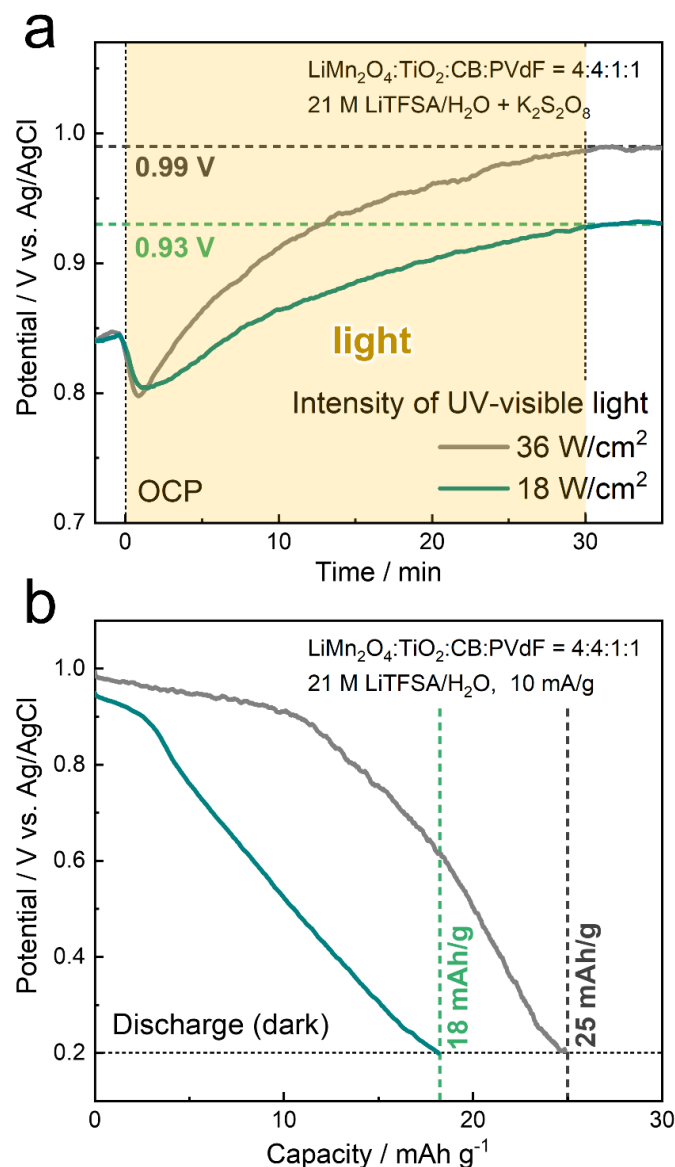**Figure S19.** (a) OCP profile for the composite electrode of $LiMn_2O_4/TiO_2$ under illumination with different intensities in the electrolyte of 21 M $LiTFSA/H_2O$ with $K_2S_2O_8$, and (b) the potential change during the subsequent discharging process at 10 mA/g after replacing the electrolyte with 21 M $LiTFSA/H_2O$ lacking electron acceptors. When the intensity was reduced to half (18 W/cm^2), the increase in potential was relatively slow and it reached only 0.93 V vs. Ag/AgCl after 30 min photocharge. The discharging capacity also decreased to 18 mAh/g, which is in between the capacities for the electrodes without illumination (14 mAh/g; Fig. S15) and with illumination at 36 W/cm^2 (25 mAh/g; Fig. 3b in the manuscript).
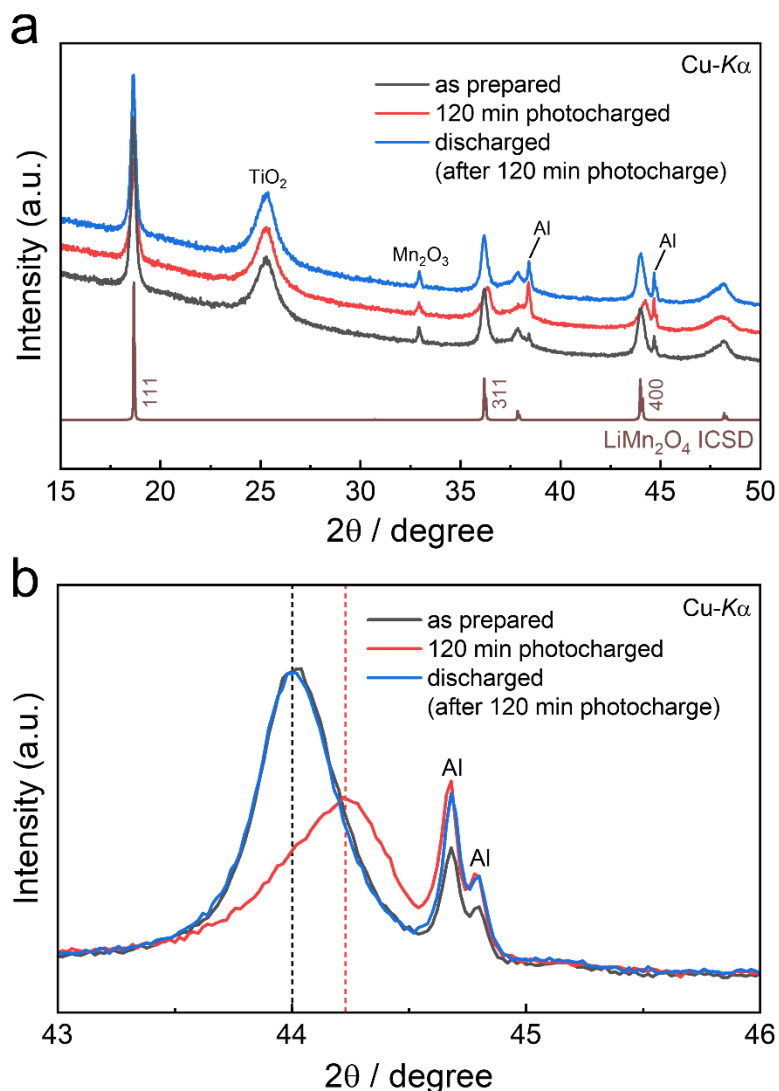
Figure S20. (a) XRD profiles for the composite electrodes of $LiMn_2O_4$ with TiO_2 before/after the photocharging for 120 min together with that after the subsequent discharge process, and (b) their enlarged view showing a diffraction from $LiMn_2O_4$ at around 44 degrees. In the top figure, there are diffraction peaks from the following four materials: $LiMn_2O_4$, TiO_2, Mn_2O_3 (impurity), and Al (current corrector), whereas only the diffraction peaks from $LiMn_2O_4$ significantly changed after the photocharging. This indicates that the charge/discharge reaction is attributed to spinel $LiMn_2O_4$. More importantly, as shown in the bottom figure, the spinel phase shows high reversibility in the bulk crystal structure. The diffraction peak broadened after the photocharging, whereas such a broadening was not observed in conventional electric charging according to a previous report.[S9] This possibly indicates that Li extraction from $LiMn_2O_4$ in the photocharging process proceeds inhomogeneously because of the high oxidation power of the holes generated in TiO_2.
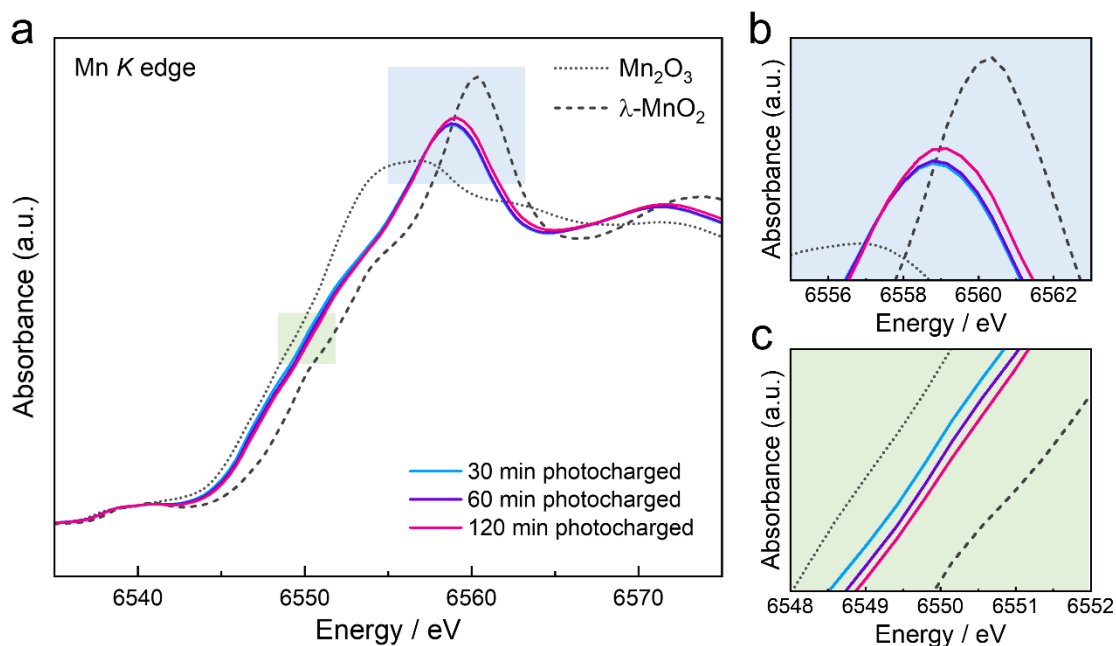
Figure S21. (a) XANES spectra for the composite electrodes of $LiMn_2O_4/TiO_2$ after the photocharging process together with those for Mn_2O_3 and λ-MnO_2 as references, and (b,c) their enlarged views. The composites were diluted with boron nitride powder to make pellets that are suitable for XANES measurements. The onset energy shifts to higher with increasing the time of photocharging, indicating the oxidation of Mn; however, the shift is apparently insufficient in considering the compositions determined by ICP analysis, according to a previous report on XANES for $LiMn_2O_4$.[S10] A possible explanation is that the Li extraction proceeds inhomogeneously and therefore highly oxidized $Li_{1-x}Mn_2O_4$ was decomposed and/or partially dissolved into the electrolyte due to its low stability. Such an inhomogeneous Li extraction was also suggested by the XRD profiles shown in Fig. S20.

References:

[S1] A. Varma, A. S. Mukasyan, A. S. Rogachev, and K. V. Manukyan, Solution combustion synthesis of nanoscale materials. *Chem. Rev.*, **116**, 14493−14586 (2016).

[S2] K. Momma and F. Izumi, VESTA 3 for three-dimensional visualization of crystal, volumetric and morphology data. *J. Appl. Crystallogr.*, **44**, 1272−1276 (2011).

[S3] F. Izumi and K. Momma, Three-dimensional visualization in powder diffraction. *Solid State Phenom.*, **130**, 15−20 (2007).

[S4] J. C. Hunter, Preparation of a new crystal form of Manganese dioxide: λ-MnO_2. *J. Solid State Chem.*, **39**, 142−147 (1981).

[S5] J. C. Knight, S. Therese, and A. Manthiram, Delithiation mechanisms in acid of spinel $LiMn_{2-x}M_xO_4$ (M = Cr, Fe, Co, and Ni) cathodes. *J. Electrochem. Soc.*, **162**, A426−A431 (2015).

[S6] G. S. Gautam, P. Canepa, A. Urban, S.-H. Bo, and G. Ceder, Influence of inversion on Mg mobility and electrochemistry in spinels. *Chem. Mater.*, **29**, 7918−7930 (2017).

[S7] A. Sclafani, M.-N. Mozzanega, and P. Pichat, Effect of silver deposits on the photocatalytic activity of titanium dioxide samples for the dehydrogenation or oxidation of 2-propanol. *J. Photochem. Photobiol. A: Chem.*, **59**, 181−189 (1991).

[S8] K. Maeda, K. Ishimaki, Y. Tokunaga, D. Lu, and M. Eguchi, Modification of wide-band-gap oxide semiconductors with cobalt hydroxide nanoclusters for visible-light water oxidation. *Angew. Chem. Int. Ed.*, **55**, 8309−8313 (2016).

[S9] K. Kanamura, H. Naito, T. Yao, and Z. Takehara, Structural change of the $LiMn_2O_4$ spinel structure induced by extraction of lithium. *J. Muter. Chem.*, **6**, 33−36 (1996).

[S10] Y. Shiraishi, I. Nakai, T. Tsubata, T. Himeda, and F. Nishikawa, In situ transmission x-ray absorption fine structure analysis of the charge−discharge process in $LiMn_2O_4$, a rechargeable lithium battery material. *J. Solid State Chem.*, **133**, 587−590 (1997).